Matrix properties of data from electrical capacitance tomography

WEIFU FANG and ELLIS CUMBERBATCH[1]
Department of Mathematics, West Virginia University, Morgantown, West Virginia 26506, USA, E-mail: wfang@math.wvu.edu; [1]*School of Mathematical Sciences, Claremont Graduate University, Claremont, California 91711, USA, E-mail: ellis.cumberbatch@cgu.edu*

Abstract. Some properties of the matrix of capacitance-data collected by the electrical capacitance tomography (ECT) technique are studied. These data are used to extract information in various industrial process applications and, in particular, about flows in pipelines. The features in the eigenvalue distribution of normalized capacitance matrices for three practical classes of permittivity distributions, namely core flows, annular flows, and stratified flows, are investigated and compared by numerical solution. It is shown that the leading eigenvalue is strongly related to the area ratio of permittivity contrast in the cross-section of the flow, while the next two eigenvalues provide a basis for distinguishing among these three classes of flows. In particular, for core and annular flows, the difference between the second and third eigenvalues is shown to be related to the eccentricity of permittivity profile. Numerical examples are presented to illustrate how the area ratio for some permittivities that do not belong to these classes can be effectively estimated.

Key words: capacitance matrix, eigenvalues, electrical capacitance tomography, parameter identification

1. Introduction

In the last decade, the electrical capacitance tomography (ECT) technique has found applications in various industrial processes, such as flow profiling in oil pipelines in the petroleum industry. As in other tomography techniques, the objective is to extract interior material profile information from surface data. One parameter that is of practical interest, among others, is the proportion or volume of a particular material flow, which is to be found without a detailed knowledge of the actual profile of the flow over the cross-section. There have been numerous studies of ECT in general by the engineering community, and some for the petroleum application in particular. See *e.g.* [1–4] and references therein.

The typical setup of an ECT sensor consists of a ring of several thin rectangular metal electrodes around the pipe or vessel, on either the exterior or interior wall of the pipe/vessel; a schematic of the cross-section of a circular sensor with exterior electrodes is shown in Figure 1. An excitation voltage is applied on one electrode (source), while the remaining electrodes (detectors) are held at zero potential, and the charge on each of the detector electrodes is measured, giving the source/detector capacitance distribution. This process continues until each electrode in the sensor system has served once as a source electrode, thus completing the collection of all mutual capacitance measurements between any pair of electrodes. Since capacitance possesses reciprocity, the mutual capacitances for a specific pair of electrodes are equal. Each self-capacitance is related to the corresponding mutual capacitances, and is

usually not measured. Hence, there are $\ell(\ell - 1)/2$ independent capacitance measurements for an ℓ-electrode ECT sensor. This array of data can be conveniently arranged in a symmetric matrix (the capacitance matrix). The purpose of this study is to investigate how some of the matrix properties of this data matrix are related to the material properties. Electrical capacitance tomography and electrical impedance tomography (EIT) are very similar in their mathematical formulation. In addition to be discussed in a large volume of engineering literature, EIT has also been the subject of many mathematical studies in the last two decades [5–8]. Each of these two problems can be formulated as an elliptic boundary-value problem for the electric potential; both problems are concerned with the recovery of the elliptic coefficient (permittivity in ECT and conductivity in EIT) from boundary measurements. In certain ideal situations, the boundary measurements by EIT can be regarded as discrete realizations of the Neumann-to-Dirichlet map, while ECT collects boundary data that are discrete realizations of the Dirichlet-to-Neumann map. The important difference between the two problems pertains to their area of applications. EIT is often used in medical applications where the main interest is in finding the exact location/shape of the inhomogeneity in the *conductive* medium, while ECT is applied more often to industrial processes such as gas/oil pipelines and gas/liquid/solid pneumatic conveyers where more interest lies in estimating the volume proportion and flow velocity of the *dielectric* materials. Generally speaking, by using EIT and ECT, we seek different interior material attributes; EIT is often employed to find local/detailed attributes such as the precise conductivity distribution of the media using many sets of data measurements, and ECT is usually applied to extract global attributes such as area ratio in the contrast of a permittivity profile from fewer sets of measurements. To the best of our knowledge, there has been little effort devoted to exploring connections between the capacitance data and global attributes in permittivity of the flow material. We note that similar problems arise from electrical resistance tomography (ERT), and in particular, matrix properties related to the material attributes for ERT are studied and used in the design of algorithms for image reconstruction in references [9, 10]. Area/size estimates of an inclusion in the conductivity using one measurement are established in reference [11].

In Section 2, we formulate the problem as an elliptic boundary-value problem for the electric potential in a circular ECT sensor with exterior electrodes. The capacitance data are often normalized, and are naturally arranged in a matrix. We then study in Section 3 the matrix properties of the capacitance matrix using the PDE model, some of which are known to the engineering community. In Section 4, we implement a finite difference numerical method for solving the boundary-value problem, and present illustrative examples for comparison of the raw and normalized capacitance matrices. We will see that normalization does enhance the presence of the material differences in the capacitance data. In Section 5, we study numerically the eigenvalue distributions of the normalized capacitance matrices. In particular, we investigate and compare the features of eigenvalue distributions for three basic classes of permittivity distributions that are most common in many industrial processes. It is shown that the leading eigenvalue is strongly related to the area ratio of the region filled by the material flow, while the next two eigenvalues contain distinctions among the three classes. Finally, we present examples on how these findings can be used to successfully estimate the area ratio for permittivities for some cases that are not exactly in these classes.

2. Model description

We assume that the axial flow velocity is slowly-varying in time, so that a time-independent model is adequate. Moreover, we assume that the flow variations are small along the axial length of the electrodes, and the capacitance measurement is interpreted as giving average cross-sectional information of the flow. Hence, we consider the cross-section, steady-state model of an ECT sensor. We also assume that the sensor is protected from other electromagnetic stray fields by a shield screen placed around the whole sensor.

   The basic assumption of our formulation is that the materials within the sensor are all linear dielectrics. That is to say, under mild electric field, the polarization is proportional to the electric field, so that the displacement is proportional to the electric field within each material.

   To be more specific, we will formulate the problem for circular pipelines with exterior electrodes. Suppose that the spatial dimensions are scaled to the exterior radius of the pipe, and hence the cross-section of the region within the sensor can be represented by the unit disk Ω, with the electrodes placed on the boundary $\partial\Omega$. Suppose that the radial thickness of the pipe wall is t_0 (typically 5~10% relative to the exterior radius of the pipe), and the cross-section of the pipe interior is described by

$$\Omega_0 = \{(x, y) : \ x^2 + y^2 < (1 - t_0)^2\}.$$

Suppose the electric field is determined by the electric potential $u(x, y)$ over the cross-section Ω, and there is no free space charge within the sensor. From Maxwell's equations [12], the potential $u(x, y)$ inside the sensor area Ω is governed by

$$\nabla \cdot (\epsilon \nabla u) = 0 \quad \text{in} \quad \Omega, \tag{1}$$

where $\epsilon = \epsilon(x, y)$ is the (relative) permittivity distribution in Ω. By assuming a two-phase flow, and scaling ϵ with the lower permittivity, we write

$$\epsilon(x, y) = \begin{cases} \epsilon_r^{(0)} & \text{in} \ \Omega \setminus \Omega_0 \quad \text{(pipe wall)}, \\ \epsilon_r & \text{in} \ D \subset \Omega_0 \ \text{(region of flow material of higher permittivity)}, \\ 1 & \text{in} \ \Omega_0 \setminus D \ \text{(region of flow material of lower permittivity)}. \end{cases} \tag{2}$$

The low permittivity flow is often gas or vacuum. This form can be easily generalized to describe more general cases of multi-phase flows. The permittivity relative to permittivity of free space for most materials in these applications is larger than 1. For example, Perspex (common material for pipes) has relative permittivity 2·56, and oil has permittivity 2·10, while for water it is about 80.

   Consider ℓ identical electrodes identified with the subsets Γ_i of $\partial\Omega$ ($i = 1, \cdots, \ell$), equally spaced on the unit circle $\partial\Omega$, and ordered counter-clockwise. Figure 1 shows a schematic of the cross-section of a 12-electrode circular ECT sensor. On each metal electrode Γ_i, the voltage is constant, and its value V_i is specified. Hence, a Dirichlet boundary condition for the potential holds on each Γ_i. On the gaps between electrodes, we assume that there is no charge on that part of the boundary, hence the homogeneous Neumann boundary condition holds for the potential. Therefore, for a given vector of applied voltage $\vec{v} = [V_1, V_2, \cdots, V_\ell]^T$, the ECT sensor will collect a vector of charges $\vec{q} = [q_1, q_2, \cdots, q_\ell]^T$, each q_k representing the charge on electrode k:

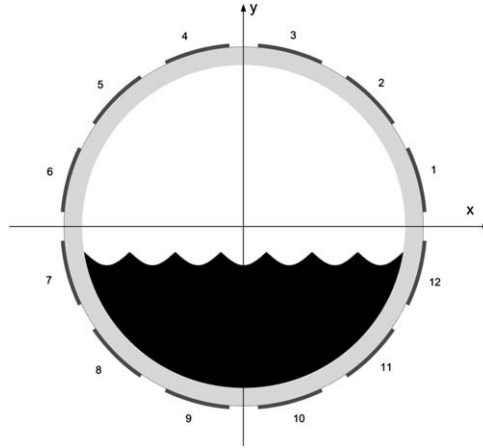$$q_k = \int_{\Gamma_k} \epsilon \frac{\partial u}{\partial \nu} \, \mathrm{d}s,$$

Figure 1. Schematic of the cross-section of a 12-electrode ECT sensor.

where u is the potential satisfying (1) with boundary conditions

$$\begin{cases} u = V_k & \text{on} \quad \Gamma_k \quad (k = 1, 2, , \cdots, \ell) \\ \epsilon \dfrac{\partial u}{\partial \nu} = 0 & \text{on} \quad \partial \Omega \setminus \cup_{k=1}^{\ell} \Gamma_k. \end{cases} \tag{3}$$

The relation between $\vec{v}$ and $\vec{q}$ is linear, and its matrix representation $C = [C_{ij}]_{\ell \times \ell}$ is known as the capacitance matrix, defined by

$$\vec{q} = C\vec{v}.$$

In addition to the geometric configuration of the sensor, the capacitance matrix depends mainly on the permittivity distribution: $C = C(\epsilon)$. It is from this matrix, C, that we would like to extract information on the permittivity distribution.

The capacitance data in C are often collected by the following experimental setup. An excitation voltage $V_j = 1$ is applied on one electrode (the 'source' (or jth) electrode) while keeping all others (the 'detector') at zero potential $V_i = 0$ ($i \neq j$), and the charges q_i on these detectors are measured. That is, $\vec{v}$ is set to $\vec{e}_j$ (the standard basis vector in R^{ℓ}) so that the measurements $\vec{q}$ are exactly the jth column of C. Specifically, if we denote by u_j the potential corresponding to the voltage excitation vector $\vec{v} = \vec{e}_j$, then we have

$$C_{ij} = \int_{\Gamma_i} \epsilon \frac{\partial u_j}{\partial \nu} ds. \tag{4}$$

The entries C_{ij} ($i \neq j$) in the capacitance matrix C are the mutual capacitance between the source electrode j and the detector electrode i, and they possess the reciprocity relation $C_{ij} = C_{ji}$. The capacitance C_{ii} is the self-capacitance, which is not measured but related to the corresponding mutual capacitances by

$$C_{ii} = -\sum_{k \neq i} C_{ik}.$$

These properties will be rigorously established in the next section; see Proposition 1. This process of collecting the capacitance data is referred to as the single-electrode excitation method. The multiple-electrode excitation method has also been investigated recently in reference [3].

In practice, because the capacitances C_{ij} are usually low-intensity signals, some normalization is needed. Common ways of normalization use the capacitances from two extreme permittivity distributions, i.e., cases with $D = \emptyset$ and $D = \Omega_0$ in (2). Let

$$\epsilon^{\text{low}}(x, y) = \begin{cases} \epsilon_r^{(0)} & \text{in } \Omega \setminus \Omega_0, \\ 1 & \text{in } \Omega_0 \end{cases}$$

and

$$\epsilon^{\text{high}}(x, y) = \begin{cases} \epsilon_r^{(0)} & \text{in } \Omega \setminus \Omega_0, \\ \epsilon_r & \text{in } \Omega_0. \end{cases}$$

Suppose $C^{\text{low}} = [C_{ij}^{\text{low}}]_{\ell \times \ell}$ and $C^{\text{high}} = [C_{ij}^{\text{high}}]_{\ell \times \ell}$ are the capacitance matrices corresponding to ϵ^{low} and ϵ^{high}, respectively. Based on either parallel or series capacitance models [13], there are two different ways of normalizing the capacitance data C_{ij} with a nontrivial $D \subset \Omega_0$,

$$\xi_{ij} = \frac{C_{ij} - C_{ij}^{\text{low}}}{C_{ij}^{\text{high}} - C_{ij}^{\text{low}}}, \tag{5}$$

and

$$\tilde{\xi}_{ij} = \frac{\dfrac{1}{C_{ij}^{\text{low}}} - \dfrac{1}{C_{ij}}}{\dfrac{1}{C_{ij}^{\text{low}}} - \dfrac{1}{C_{ij}^{\text{high}}}}. \tag{6}$$

We denote the corresponding matrices by $\Xi = [\xi_{ij}]_{\ell \times \ell}$ and $\tilde{\Xi} = [\tilde{\xi}_{ij}]_{\ell \times \ell}$, respectively. Note that these normalized capacitance matrices Ξ and $\tilde{\Xi}$ reduce to the zero matrix when $D = \emptyset$, and to the matrix of all 1's when $D = \Omega_0$, although the entries ξ_{ij} or $\tilde{\xi}_{ij}$ are not necessarily between 0 and 1. These normalizations are expected to reduce the effect of the geometric setup and to enhance the presence of the material with permittivity $\epsilon_r > 1$.

3. Properties of the capacitance matrix

In this section, we establish some properties of the capacitance matrix C. Some of these properties are well known in the engineering literature (*e.g.* [3]). Here, we show how they can be derived from the PDE model.

The boundary-value problem described by (1) with (3) can be stated in the weak form. We say that u is an H^1 weak solution to (1) with (3) if $u \in H^1(\Omega)$ satisfies

$$u|_{\Gamma_k} = V_k \quad (k = 1, \cdots, \ell) \quad \text{and} \quad \iint\limits_{\Omega} \epsilon \nabla u \cdot \nabla \phi \, \mathrm{d}x\mathrm{d}y = 0 \quad \text{for all } \phi \in \mathcal{V}, \tag{7}$$

where

$$\mathcal{V} \equiv \{\phi \in H^1(\Omega) : \ \phi|_{\cup_{k=1}^{\ell} \Gamma_k} = 0\}.$$

Existence of a unique weak solution can be established in standard fashion. It is known that the derivatives of the solution possess singularities near the joins between Dirichlet and Neumann

boundary conditions. Since $\epsilon\nabla u$ is divergence-free, $\epsilon\nabla u \cdot \nu$ is in $H^{-1/2}(\partial\Omega)$, and satisfies the Green's identity

$$\iint\limits_{\Omega} \epsilon\nabla u \cdot \nabla\phi \; \mathrm{d}x\mathrm{d}y = \int_{\cup_{k=1}^{\ell}\Gamma_k} \epsilon\frac{\partial u}{\partial\nu}\phi \; \mathrm{d}s \quad \text{for all } \phi \in H^1(\Omega), \tag{8}$$

where the right-hand side is understood as the dual pair of $H^{-1/2}(\partial\Omega)$ and $H^{1/2}(\partial\Omega)$. In particular, the capacitance C_{ij} in (4) is the numerical value of the dual pair on particular test functions ϕ which have trace value 1 on Γ_i, and 0 on the other Γ_k's.

We can establish the maximum principle for the weak solution u without requiring further analytic regularities of the solution. Let $\underline{V} = \min_k V_k$ and $\overline{V} = \max_k V_k$. For $\phi = \min(u, \underline{V})$, we see that $\phi \in \mathcal{V}$ and $\nabla\phi = \nabla u$. Hence $|\nabla\phi| = 0$ by (7), and thus $\phi = 0$ almost everywhere (a.e.) in Ω. Therefore $u \geq \underline{V}$ a.e. in Ω. Similarly we can show that $u \leq \overline{V}$ a.e. in Ω. Hence, the weak solution $u \in H^1(\Omega)$ satisfies the maximum principle

$$\min_k V_k \leq u(x, y) \leq \max_k V_k \quad \text{a.e. in } \Omega. \tag{9}$$

In Equation (8) for u_j, if we set $\phi = u_i$, we see immediately that the capacitance C_{ij} as given in (4) can be expressed as

$$C_{ij} = \iint\limits_{\Omega} \epsilon\nabla u_i \cdot \nabla u_j \; \mathrm{d}x\mathrm{d}y, \tag{10}$$

and the capacitance matrix $C = [C_{ij}]$ is expressed conveniently as

$$C = \iint\limits_{\Omega} \epsilon(\nabla\vec{u})(\nabla\vec{u})^T \; \mathrm{d}x\mathrm{d}y, \tag{11}$$

where we denote

$$\vec{u} = \begin{bmatrix} u_1 \\ u_2 \\ \vdots \\ u_\ell \end{bmatrix} \quad \text{and} \quad \nabla\vec{u} = \begin{bmatrix} \partial_x u_1 & \partial_y u_1 \\ \partial_x u_2 & \partial_y u_2 \\ \vdots & \vdots \\ \partial_x u_\ell & \partial_y u_\ell \end{bmatrix}.$$

This alternative representation of the capacitance data, (10) or (11), is helpful in establishing the following results on the properties of matrix C.

PROPOSITION 1. *The capacitance matrix C is symmetric, semi-positive definite with rank $\ell - 1$, and its entries satisfy*

$$C_{ii} > 0, \quad \sum_{k=1}^{\ell} C_{kj} = \sum_{k=1}^{\ell} C_{ik} = 0 \quad \text{for} \quad i, j = 1, 2, \cdots, \ell. \tag{12}$$

If, in addition, the solution u_i has continuous normal derivative up to each Γ_j, then $C_{ij} < 0$ for $i \neq j$.

Proof. Formula (11) clearly shows that the capacitance matrix C is symmetric indeed. In addition,

$$\vec{\zeta}^T C \vec{\zeta} = \iint\limits_{\Omega} \epsilon\nabla(\sum_{k=1}^{\ell} \zeta_k u_k) \cdot \nabla(\sum_{k=1}^{\ell} \zeta_k u_k) \; \mathrm{d}x\mathrm{d}y \geq 0 \quad \text{for any} \quad \vec{\zeta} \in R^\ell, \tag{13}$$

which implies the semi-positive definiteness of C.

Next, we let $w(x, y) = \sum_{k=1}^{\ell} u_k(x, y) - 1$. Then $w \in \mathcal{V}$ and, from (7) for u_j,

$$\iint_{\Omega} \epsilon \nabla u_j \cdot \nabla w \, \mathrm{d}x\mathrm{d}y = 0, \quad j = 1, 2, \cdots, \ell. \tag{14}$$

Summing up (14) for j from 1 to ℓ yields

$$\iint_{\Omega} \epsilon |\nabla w|^2 \, \mathrm{d}x\mathrm{d}y = 0,$$

which implies that $w \equiv 0$ a.e. in Ω. Hence, for $\vec{\eta} = [1, 1, \cdots, 1]^T$, we have

$$C\vec{\eta} = \iint_{\Omega} \epsilon (\nabla \vec{u})(\nabla \vec{u})^T \vec{\eta} \, \mathrm{d}x\mathrm{d}y = \iint_{\Omega} \epsilon (\nabla \vec{u})(\nabla w)^T \, \mathrm{d}x\mathrm{d}y = \vec{0}. \tag{15}$$

That is, $\vec{\eta} \neq \vec{0}$ is in the nullspace of C. Thus C is singular and rank$(C) \leq \ell - 1$. On the other hand, for any vector $\vec{\zeta}$ in the nullspace of C, we see from (13) that

$$0 = \iint_{\Omega} \epsilon \nabla(\sum_{k=1}^{\ell} \zeta_k u_k) \cdot \nabla(\sum_{k=1}^{\ell} \zeta_k u_k) \, \mathrm{d}x\mathrm{d}y.$$

Therefore

$$\iint_{\Omega} |\nabla(\sum_{k=1}^{\ell} \zeta_k u_k)|^2 \mathrm{d}x\mathrm{d}y = 0, \quad \text{hence} \quad \sum_{k=1}^{\ell} \zeta_k u_k(x, y) \equiv \alpha \text{ (constant)}.$$

On each Γ_k, $\sum_{i=1}^{\ell} \zeta_i u_i(x, y) = \zeta_k$. Therefore $\zeta_k = \alpha$ for all $k = 1, 2, \cdots, \ell$. That is, $\vec{\zeta} = \alpha\vec{\eta}$. Thus we have shown that the nullspace of C is exactly the one-dimensional space spanned by $\vec{\eta}$. Therefore, rank$(C) = \ell - 1$.

The positivity of the main diagonal entries (self capacitance) $C_{jj} > 0$ follows immediately from (10). Relation (15) and the symmetry of C also imply that the sum over each row or column of C is zero. Thus, (12) is established. With the additional continuity assumption on the normal derivative of the solution, we can show that all other capacitances $C_{ij} < 0$ for $i \neq j$. Indeed, from the maximum principle (9), we have $0 \leq u_j \leq 1$ in Ω. On each Γ_i with $i \neq j$, $u_j = 0$ and hence $\dfrac{\partial u_j}{\partial \nu} \leq 0$. Therefore $C_{ij} = \int_{\Gamma_i} \epsilon \dfrac{\partial u_j}{\partial \nu} \mathrm{d}s \leq 0$. If $C_{ij} = 0$, then $\dfrac{\partial u_j}{\partial \nu} = 0$ on Γ_i, and thus u_j would have zero Cauchy data on Γ_i, which would in turn lead to $u_j \equiv 0$ throughout Ω, a contradiction. Therefore, $C_{ij} < 0$ for $i \neq j$. $\square$

Therefore, for an ℓ-electrode sensor, the $\ell(\ell-1)/2$ independent capacitance measurements comprise the entries of the upper or lower triangle of C; the other half of C is filled by symmetry, and the diagonal entries are computed by (12).

The capacitance matrix clearly depends on how the electrodes are numbered. For two different numberings of the electrodes, the relation between the corresponding capacitance matrices can be easily derived from formula (11).

PROPOSITION 2. *In the same geometric setting, suppose that C and C′ are the capacitance matrices corresponding to two different numberings of the electrodes, say $(1, 2, \cdots, \ell)$ and $(i_1, i_2, \cdots, i_\ell)$, respectively. Then*

$$C' = PCP^T = PCP^{-1}, \tag{16}$$

where P is the permutation matrix in $[i_1, i_2, \cdots, i_\ell]^T = P[1, 2, \cdots, \ell]^T$. Hence, C and C′ have the same eigenvalue distribution.

This proposition has useful implications. If the permittivity distribution ϵ' is the result of rotating the permittivity ϵ by an integer multiple of $2\pi/\ell$ angle, then the corresponding capacitance matrices also obey relation (16). Specifically, if

$$\epsilon'(x, y) = \epsilon'(r\cos\theta, r\sin\theta) = \epsilon(r\cos(\theta - k\frac{2\pi}{\ell}), r\sin(\theta - k\frac{2\pi}{\ell})) \tag{17}$$

for some $1 \le k \le \ell - 1$, then the capacitance matrix C' corresponding to ϵ' is related to the capacitance matrix C corresponding to ϵ by (16), with P being the permutation matrix that shifts $[1, 2, \cdots, \ell]^T$ to $[k, \cdots, \ell, 1, \cdots, k - 1]^T$. In particular, C and C' have the same eigenvalue distribution. Since such a rotation does not change the area of D, we should search for properties of the matrix that are invariant under such similarity transformations to serve as an indicator for the area $|D|$. Eigenvalues are obvious candidates.

In the following, we assume that the electrodes are ordered on the unit circle counterclockwise, as depicted in Figure 1. We will consider further the case of radial symmetric permittivities, such as central core flows and central annular flows. In fact, all we require is that ϵ is radially symmetric with respect to the the ℓ electrodes: $\epsilon' \equiv \epsilon$ in (17) for all k. This includes also shapes like ℓ-polygons. Note that, in such cases, all the self-capacitances C_{ii} are equal.

PROPOSITION 3. *If ϵ is radially symmetric with respect to the ℓ electrodes, then the capacitance matrix C is a symmetric circulant matrix, and its real eigenvalues $(\lambda_0, \lambda_1, \cdots, \lambda_{\ell-1})$ satisfy*

$$\lambda_0 = 0 < \lambda_k = \lambda_{\ell-k} < 2C_{ii} \quad (k = 1, 2, \cdots, \ell - 1).$$

Proof. Let $\vec{c} = [c_0, c_1, \cdots, c_{\ell-1}]^T = [C_{11}, C_{21}, \cdots, C_{\ell 1}]^T$ be the vector of capacitances with number 1 electrode as the source electrode. This will be the first column of the capacitance matrix C. From (12), we have

$$c_0 > 0, \quad c_k < 0 \ (k = 1, 2, \cdots, \ell - 1) \quad \text{and} \quad c_0 = -\sum_{k=1}^{\ell-1} c_k. \tag{18}$$

The self-capacitances C_{ii} are all equal to c_0. Since electrode $k + 1$ and electrode $\ell - k + 1$ are in symmetric positions with respect to the source electrode 1, and likewise the permittivity, we can easily see that the mutual capacitances of the two pairs $(1, k + 1)$ and $(1, \ell - k + 1)$ are equal,

$$c_k = c_{\ell-k} \quad \text{for } k = 1, \cdots, \ell - 1. \tag{19}$$

The second column of C consists of the capacitances when the number 2 electrode is the source electrode. But clearly this vector would be exactly $\vec{c}$, except for one 'downshift' in the entries: $[c_{\ell-1}, c_0, c_1, \cdots, c_{\ell-2}]^T$. The following columns of C have the same property: each column is the one-position downshift of its previous column, wrapping the last entry back to the beginning. In fact this is also true for rows of C. Therefore, C indeed is a circulant matrix, generated by $\vec{c}$. Relation (19) or Proposition 1 implies that C is also symmetric.

A nice property of a circulant matrix is that the vector consisting of the eigenvalues is the discrete Fourier transform of its generating vector [14]:

$$\begin{bmatrix} \lambda_0 \\ \lambda_1 \\ \lambda_2 \\ \vdots \\ \lambda_{\ell-1} \end{bmatrix} = \begin{bmatrix} 1 & 1 & 1 & \cdots & 1 \\ 1 & w & w^2 & \cdots & w^{\ell-1} \\ 1 & w^2 & w^4 & \cdots & w^{2(\ell-1)} \\ \vdots & \vdots & \vdots & \ddots & \vdots \\ 1 & w^{\ell-1} & w^{2(\ell-1)} & \cdots & w^{(\ell-1)^2} \end{bmatrix} \begin{bmatrix} c_0 \\ c_1 \\ c_2 \\ \vdots \\ c_{\ell-1} \end{bmatrix}$$

where $w = \mathrm{e}^{-2\pi\mathrm{i}/\ell}$. Because of (18), we see immediately that $\lambda_0 = 0$. Due to the symmetry (19), the other eigenvalues are real and satisfy the relation $\lambda_k = \lambda_{\ell-k}$. Notice that each λ_k is of the form $c_0 + \sum_{k=1}^{\ell-1} \alpha_k c_k$ with coefficients $\alpha_k \in [-1, 1]$, not all equal. Therefore, each eigenvalue has a strict lower bound of $c_0 + \sum_{k=1}^{\ell-1} c_k = 0$ and a strict upper bound of $c_0 + \sum_{k=1}^{\ell-1}(-c_k) = 2c_0 = 2C_{ii}$, both by (18). $\square$

Since normalizations (5) and (6) are done component-wise for the matrix C, some properties of C, such as symmetry and circulancy, can be carried over to the normalized matrices Ξ and $\tilde{\Xi}$. But most other properties, such as positive definiteness and rank, cannot be carried over in general. We summarize the results on the normalized matrices below.

PROPOSITION 4. *Let Ξ and $\tilde{\Xi}$ be the normalized capacitance matrices defined by (5) and (6), respectively. Then*

1. *Ξ and $\tilde{\Xi}$ are symmetric.*
2. *If two permittivity distributions are discrete rotations of each other as in (17), then their corresponding normalized capacitance matrices Ξ (or $\tilde{\Xi}$) are related by a permutation matrix as in (16). Hence, they have the same eigenvalue distribution.*
3. *If ϵ is radial symmetric with respect to the ℓ electrodes, then Ξ and $\tilde{\Xi}$ are also circulant, and each has at most $[\frac{\ell+1}{2}] + 1$ distinct eigenvalues.*

It will be seen in our numerical examples that the normalized matrices Ξ and $\tilde{\Xi}$ are usually non-singular when $D \neq \emptyset$, but not positive-definite. A detailed discussion of the eigenvalue distributions of Ξ and $\tilde{\Xi}$ will be presented in Section 5.

4. Numerical solution

When the gaps between the electrodes are zero, it is possible to solve the problem (1–3) analytically by elementary methods (separation of variables, conformal mapping) for special cases of permittivities such as those corresponding to central core and central annular flows [15]. However, for cases of nonzero gaps or other flow configurations, these solution methods no longer apply, and we must rely on numerical solutions. In this section, we implement a standard 5-point finite difference scheme for the equations in polar coordinates, and present some illustrative examples.

The boundary-value problem (1) with (3) in polar coordinates (r, θ), with the usual numbering for the electrodes, takes the form

$$
\begin{cases}
r\dfrac{\partial}{\partial r}\left(r\epsilon\dfrac{\partial u}{\partial r}\right) + \dfrac{\partial}{\partial \theta}\left(\epsilon\dfrac{\partial u}{\partial \theta}\right) = 0 \ \ \text{in} \ \ \{(r,\theta): \ 0 \le r < 1, \ 0 \le \theta < 2\pi\}, \\[2mm]
\hspace{3cm} u = V_k \ \ \text{on} \ \ \{(r,\theta): \ r=1, \ \theta \in I_k\} \ \ (k = 1, \cdots, \ell), \quad (20) \\[2mm]
\hspace{2.5cm} \epsilon\dfrac{\partial u}{\partial r} = 0 \ \ \text{on} \ \ \{(r,\theta): \ r=1, \ \theta \in [0, 2\pi) \setminus \bigcup_{k=1}^{\ell} I_k\}
\end{cases}
$$

where I_k denotes the angular interval for the kth electrode on $r = 1$,

$$
I_k = [(k-1)\frac{2\pi}{\ell} + \frac{\delta}{2}, k\frac{2\pi}{\ell} - \frac{\delta}{2}] \quad \text{for} \ \ k = 1, 2, \cdots, \ell,
$$

and δ is the gap angle between electrodes.

Given two integers n and m, we set up a finite-difference grid

$$
(r_i, \theta_j) = (i\,\Delta r, \ j\,\Delta\theta) \quad \text{with} \quad \Delta r = \frac{1}{n}, \ \ \Delta\theta = \frac{2\pi}{m},
$$

for $i = 0, 1, \cdots, n$ and $j = 0, 1, \cdots, m$. On each polar 'pixel', we assume the permittivity is a constant:

$$
\epsilon(r, \theta) = \epsilon_{i+\frac{1}{2}, j+\frac{1}{2}} \quad \text{on} \ \ [r_i, r_{i+1}] \times [\theta_j, \theta_{j+1}],
$$

for $0 \le i \le n-1$ and $0 \le j \le m-1$. The central difference approximation of the equation at nodal point (i, j) reads

$$
\frac{r_i}{(\Delta r)^2}\left((r\epsilon)_{i-\frac{1}{2},j}U_{i-1,j} - ((r\epsilon)_{i-\frac{1}{2},j} + (r\epsilon)_{i+\frac{1}{2},j})U_{ij} + (r\epsilon)_{i+\frac{1}{2},j}U_{i+1,j}\right)
$$

$$
+ \frac{1}{(\Delta\theta)^2}\left(\epsilon_{i,j-\frac{1}{2}}U_{i,j-1} - (\epsilon_{i,j-\frac{1}{2}} + \epsilon_{i,j+\frac{1}{2}})U_{ij} + \epsilon_{i,j+\frac{1}{2}}U_{i,j+1}\right) = 0
$$

$(1 \le i \le n-1, \ 1 \le j \le m-1)$, with boundary conditions discretized accordingly. At $r = 0$ $(i = 0)$, we use the condition $\frac{\partial u}{\partial r} = 0$, and at $\theta = 2\pi$ $(j = 0$ and $j = m)$, we use the periodicity $u(r, 0) = u(r, 2\pi)$ and $u_\theta(r, 0) = u_\theta(r, 2\pi)$,

$$
U_{1,j} = U_{0,j} = U_{0,0}, \quad U_{i,0} = U_{i,m} \quad \text{and} \quad U_{i,1} = U_{i,m+1}.
$$

In the following numerical example, we choose model parameters

$$
\ell = 12, \quad \delta = \frac{\pi}{20} = 9° \ (\text{gap angle}), \quad t_0 = 0{\cdot}1, \quad \epsilon_r^{(0)} = 2{\cdot}56, \quad \epsilon_r = 2{\cdot}1,
$$

$$
D = \{(x, y) \in \Omega_0 : \ x^2 + (y + 0{\cdot}45)^2 \le 0{\cdot}4^2\},
$$

and a grid with

$$
\Delta r = \frac{1}{n} = \frac{1}{50} \quad \text{and} \quad \Delta\theta = \frac{2\pi}{m} = \frac{2\pi}{240}.
$$

The permittivity distribution ϵ and equipotential lines of u_1 (single source electrode at electrode 1) are depicted in Figure 2.
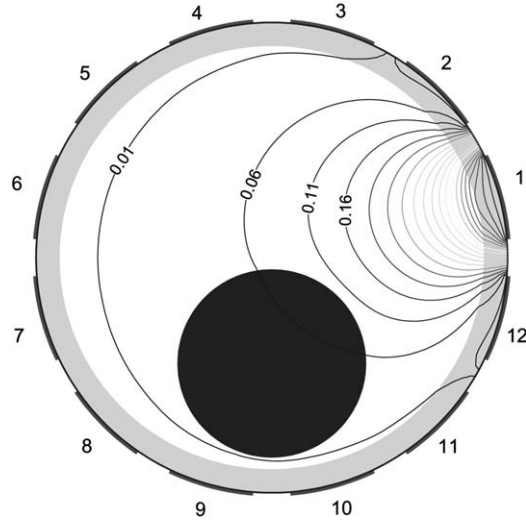
Figure 2. Permittivity distribution $\epsilon(x, y)$ and equipotential lines for the potential $u_1(x, y)$ when electrode 1 is the single source electrode.

The calculation was repeated with the source electrode moved around, so that the capacitance matrix can be obtained. The capacitance data are presented in Figure 3, where the raw capacitance matrix C is on the top row, the normalized capacitance matrix Ξ, (5), in the middle, and the normalized capacitance matrix $\tilde{\Xi}$, (6), on the bottom. In each case, the entries of the matrix are plotted column after column on the left, while the entries are presented as the heights at their matrix positions on the right. It is clear that normalization does enhance the capacitances from electrodes 9 and 10, which are closest to the flow area D.

5. Eigenvalues of normalized capacitance matrices

In this section, we use the numerical method described in Section 4 to investigate numerically the relation between the eigenvalue distribution of the normalized capacitance matrices Ξ and $\tilde{\Xi}$ and the permittivity distribution ϵ. We will restrict ourselves to certain classes of permittivity distributions that are common and important in applications. These are:

$$\text{Stratified flows:} \quad D = \{(x, y) : \quad x \cos\theta_0 + y \sin\theta_0 \geq d\}, \tag{21}$$

$$\text{Core flows:} \quad D = \{(x, y) : \quad (x - d_0 \cos\theta_0)^2 + (y - d_0 \sin\theta_0)^2 \leq r_0^2\}, \tag{22}$$

$$\text{Annular flows:} \quad D = \{(x, y) : \quad (x - d_0 \cos\theta_0)^2 + (y - d_0 \sin\theta_0)^2 \geq r_0^2\}, \tag{23}$$

where the parameters θ_0, d, d_0, and r_0 satisfy the constraints

$$0 \leq \theta_0 < 2\pi, \quad |d| \leq 1 - t_0, \quad d_0 \geq 0, \quad r_0 \geq 0, \quad \text{and} \quad d_0 + r_0 \leq 1 - t_0.$$

These three classes of permittivity distributions are depicted in Figure 4.

In the following, we investigate numerically the unique features of the eigenvalue distribution of the normalized capacitance matrix Ξ or $\tilde{\Xi}$ for each of these three classes of permittivity distributions, so that these features can be used for the purpose of parameter identification/estimation.
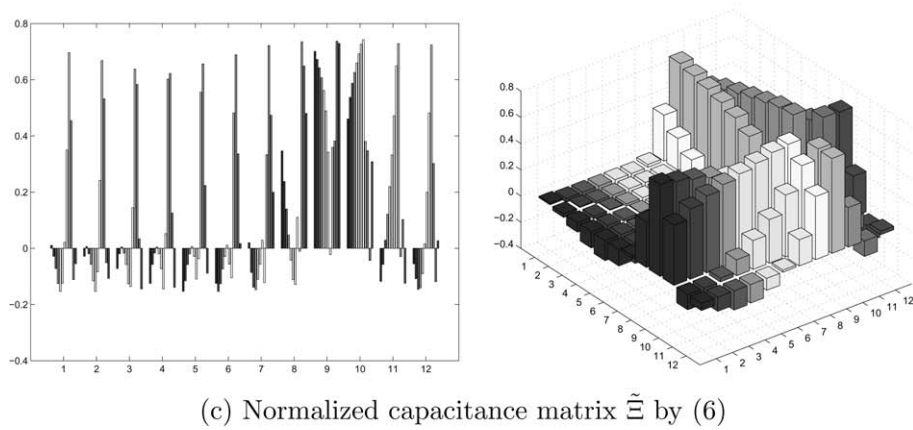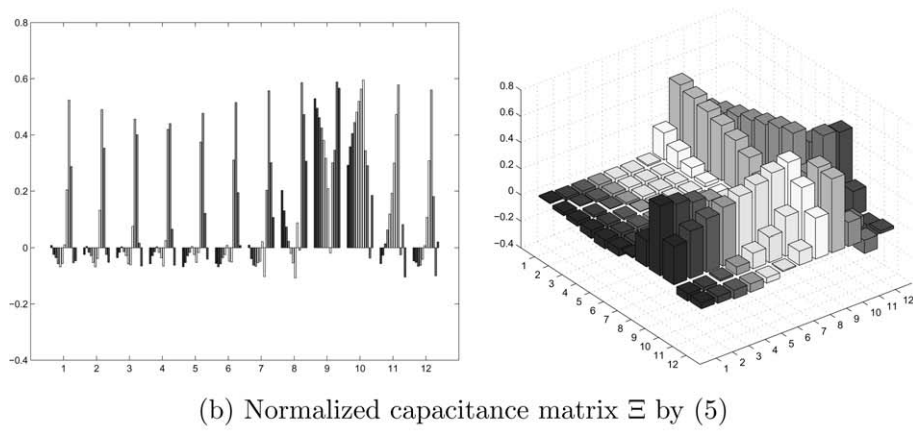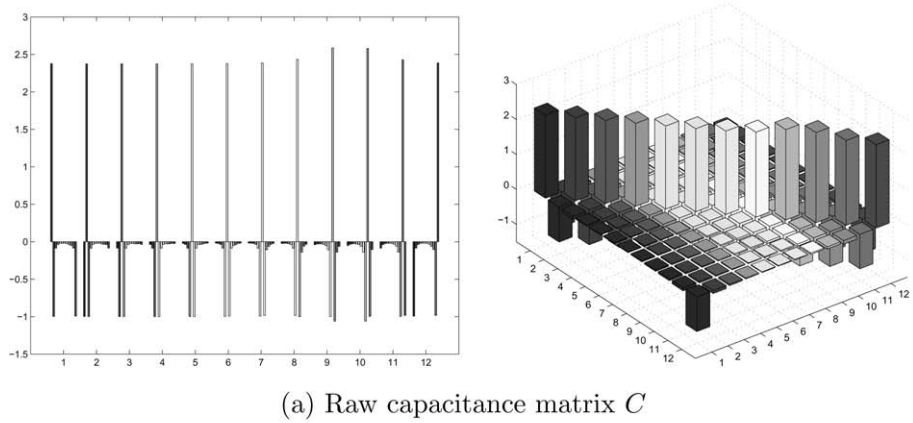
(a) Raw capacitance matrix C

(b) Normalized capacitance matrix Ξ by (5)

(c) Normalized capacitance matrix $\tilde{\Xi}$ by (6)

Figure 3. The raw capacitance matrix C and normalized capacitance matrices Ξ and $\tilde{\Xi}$, for the permittivity distribution shown in Figure 2.
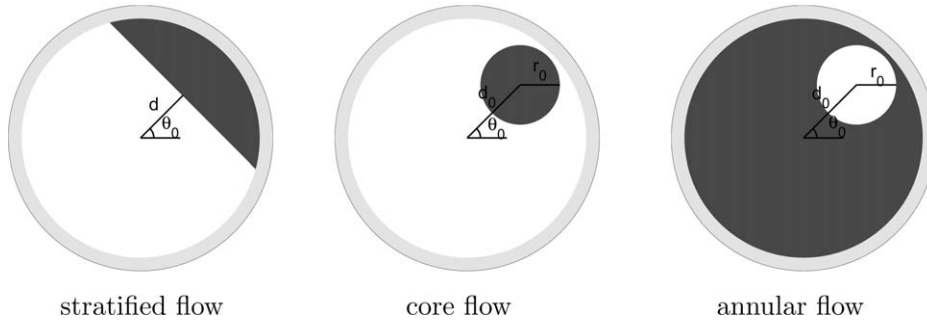
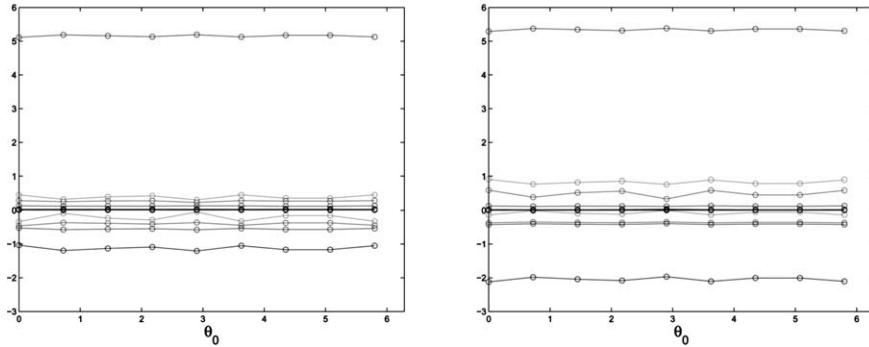*Figure 4.* The three common classes of permittivity distributions.

Figure 5. The eigenvalues of Ξ (left) and $\tilde{\Xi}$ (right) plotted against θ_0 for the stratified flows (21), with $d = 0.4$.

Example 1: *Independence on the angular position* θ_0. From Proposition 4, we know that, for each of these classes, the eigenvalues of Ξ and $\tilde{\Xi}$ are invariant under discrete increments of θ_0 (integer multiples of $2\pi/\ell$). Our numerical experiments show that the eigenvalues remain relatively unchanged as θ_0 varies through values that are not integer multiples of $2\pi/\ell$. In Figure 5 we plot the eigenvalues for the stratified flows (21) with θ_0 taking the values $3k\pi/13$ for $k = 0, 1, \cdots, 8$. Clearly the eigenvalues almost remain the same for these values of θ_0, with small fluctuations due to likely numerical errors. It is also the case for the core flows (22) and annular flows (23). Therefore, in studying the eigenvalues of Ξ and $\tilde{\Xi}$ for these three classes, we can eliminate θ_0 as a parameter. Hence, the core flows and annular flows are characterized by r_0 and d_0, while the stratified flows are determined by only one parameter, d.

Example 2: *Eigenvalue distributions of stratified flows.* In this example, we illustrate the eigenvalue distribution of Ξ and $\tilde{\Xi}$ for the class of stratified flows (21). We set $\theta_0 = 0$ and vary d from -0.8 to 0.8. In Figure 6, we plot the 12 eigenvalues of Ξ and $\tilde{\Xi}$ against the area ratio $|D|/|\Omega_0|$. We see that the leading eigenvalue of either Ξ or $\tilde{\Xi}$ is a robust indicator of the area ratio, and can be used to identify the only parameter d within the class.

Example 3: *Eigenvalue distributions of core flows.* There are two parameters in this class: the radius r_0 and the eccentricity d_0. When $d_0 = 0$, the permittivity distributions are radially symmetric. Hence Ξ and $\tilde{\Xi}$ are circulant, and there are exactly 7 distinct eigenvalues in these examples. As d_0 becomes nonzero, symmetry is lost, and so is the multiplicity of the eigenvalues. The eigenvalues are plotted in Figure 7 against the area ratio $|D|/|\Omega_0|$, for both concentric case (top) and eccentric case (bottom).
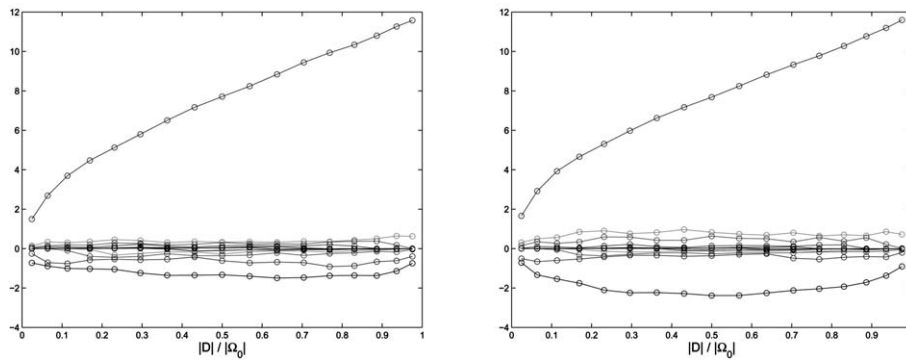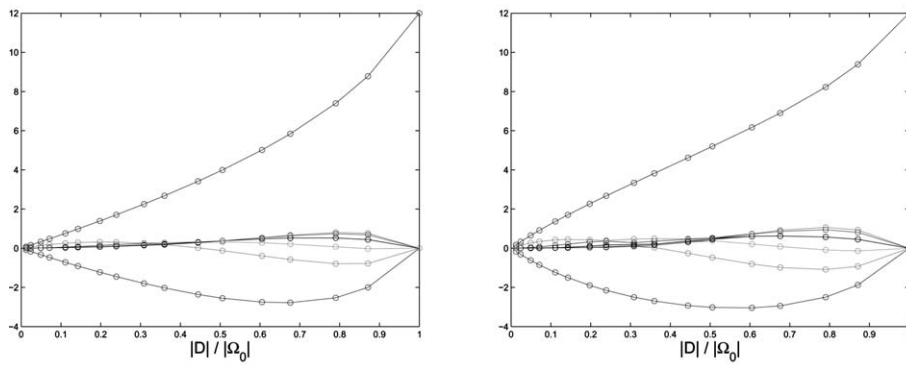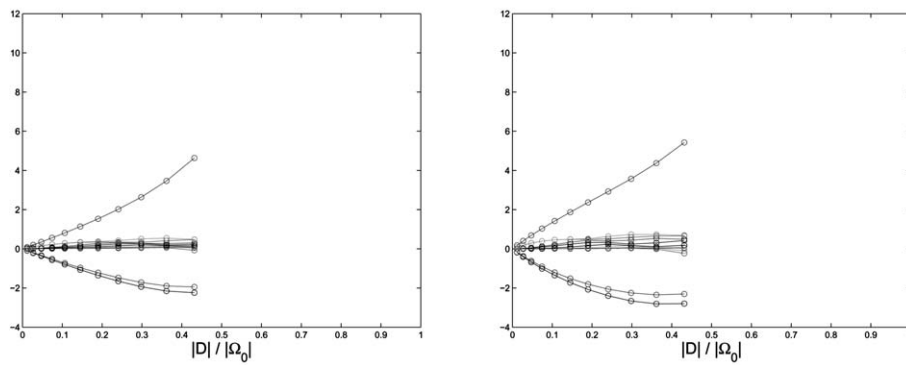
Figure 6. The eigenvalues of Ξ (left) and $\tilde{\Xi}$ (right) plotted against the area ratio $|D|/|\Omega_0|$ for the stratified flows (21), with $\theta_0 = 0$.

(a) Case of concentric core flows: $d_0 = 0$.

(b) Case of eccentric core flows: $d_0 = 0.3$.

Figure 7. The eigenvalues of Ξ (left) and $\tilde{\Xi}$ (right) plotted against the area ratio $|D|/|\Omega_0|$ for the core flows (22), with $\theta_0 = 0$.
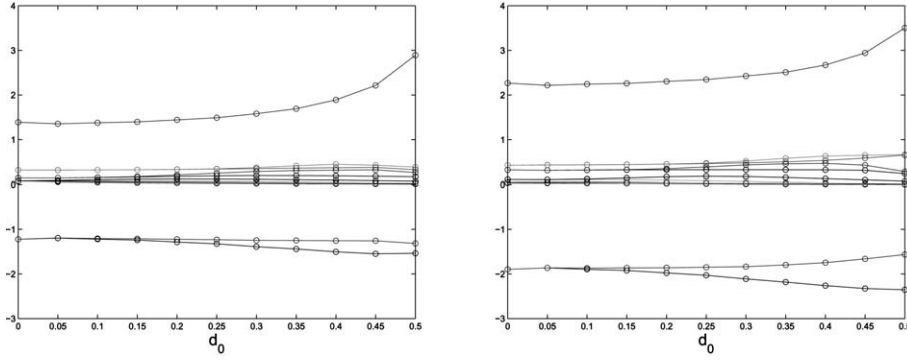
Figure 8. The eigenvalues of Ξ (left) and $\tilde{\Xi}$ (right) plotted against the eccentricity d_0 for the core flows (22), with $r_0 = 0.4$ and $\theta_0 = 0$.

For convenience, let us label the eigenvalues in descending order of absolute values:

$$|\tau_1| \geq |\tau_2| \geq \cdots \geq |\tau_\ell|.$$

Note that the leading eigenvalue τ_1 is positive and simple, and nearly linear in the area ratio, while the second largest in absolute value is negative and has multiplicity 2 ($\tau_2 = \tau_3 < 0$). As the eccentricity d_0 becomes nonzero, τ_2 and τ_3 remain negative but grow apart. To better see the effect of the eccentricity d_0, in Figure 8 we plot the eigenvalues as d_0 varies while r_0 is held fixed. Note that in this case the area ratio is fixed (Figure 8). Hence, we see that the leading eigenvalue τ_1 alone would not be able to accurately describe the area ratio $|D|/|\Omega_0|$; it should be adjusted by eccentricity. Moreover, the eigenvalue distributions are almost identical for all small values of eccentricity d_0, which seems to indicate that central flows are more difficult for circular ECT sensor to locate/detect.

Next, we investigate the use of the leading eigenvalue τ_1 and the difference $|\tau_2 - \tau_3|$ as joint indicators of the core flows (22). Over the parameter domain

$$\{(d_0, \rho) : \ d_0 \geq 0, \ \ \rho \geq 0, \ \ d_0 + 0 \cdot 9\sqrt{\rho} \leq 0 \cdot 9\},$$

where ρ represents the area ratio $\rho = |D|/|\Omega_0| = r_0^2/0 \cdot 9^2$, we plot the surfaces of τ_1 and $|\tau_2 - \tau_3|$ of $\tilde{\Xi}$ in Figure 9. We can see that, indeed, for most cases, these two parameters are capable of identifying both the eccentricity and area ratio of a core flow, except when either one is small (*i.e.*, when the core is small or near the center). We present the calculations for $\tilde{\Xi}$ only, since these features are slightly more enhanced in $\tilde{\Xi}$ than in Ξ.

Example 4: *Eigenvalue distributions of annular flows.* We study the case of annular flows described by (23). The eigenvalues are plotted as functions of the area ratio $|D|/|\Omega_0|$ in Figure 10, for the concentric case in (a) and an eccentric case in (b). As in the case of core flows, the leading eigenvalue τ_1 is positive, simple, and nearly linear in the area ratio, and τ_2 and τ_3 are equal for concentric flows and distinct for eccentric ones.

However, one significant difference here is that τ_2 and τ_3 are positive. Moreover, we see that τ_1 remains almost unchanged as eccentricity d_0 varies in Figure 11. Therefore, the leading eigenvalue τ_1 seems to be a strong indicator of the area ratio for this class of permittivities, independent of eccentricity. The two surfaces τ_1 and $|\tau_2 - \tau_3|$ are presented in Figure 12, over the parameter domain

$$\{(d_0, \rho) : \ d_0 \geq 0, \ \ 0 \leq \rho \leq 1, \ \ d_0 + 0 \cdot 9\sqrt{\rho} \geq 0 \cdot 9\}.$$
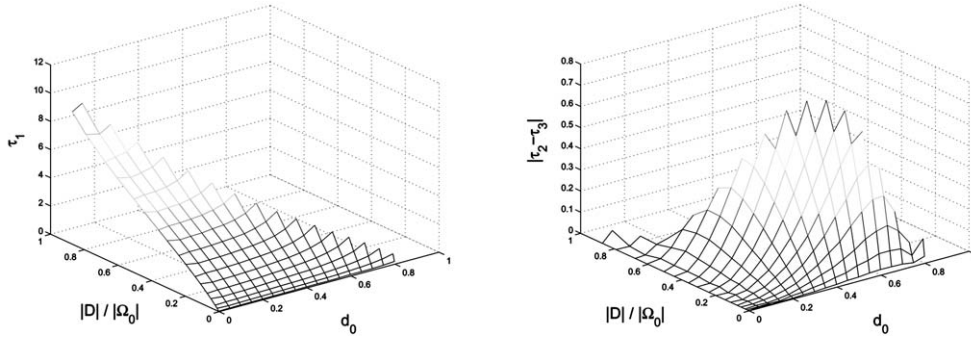
Figure 9. Surfaces of τ_1 (left) and $|\tau_2 - \tau_3|$ (right) for $\tilde{\Xi}$, as functions of eccentricity d_0 and area ratio $|D|/|\Omega_0|$, for the core flows (22).

If desired, the difference $|\tau_2 - \tau_3|$ can be used to help identify the eccentricity, in addition to the area ratio. However, it seems difficult to do so when d_0 is small and the area ratio is large, which is the case when the void is near the center and small. In particular, from Figure 11, the capacitance data seem indifferent to the location of the void near the center of the sensor.

From our numerical results, it is clear that the first few leading eigenvalues do provide distinctive and descriptive information about the permittivity distributions among the three basic classes (21–23). We summarize our observations as follows. For all three classes, the largest eigenvalue τ_1 is positive and simple, and nearly linear in the area ratio $|D|/\Omega_0|$. The next two eigenvalues τ_2 and τ_3 contain information that distinguishes the permittivity distributions among the three classes:

core flows: $\tau_2 \approx \tau_3$ and both are negative,

annular flows: $\tau_2 \approx \tau_3$ and both are positive,

stratified flows: τ_2 and τ_3 are more likely to have opposite signs.

Note that when the area $|D|$ is small, these characterizations of the flow types may not be necessarily accurate. In most cases, these descriptions provide us with criteria to successfully identify the parameters about the permittivity within these classes, and sometimes help produce good approximations to permittivities that are not exactly in any one of these classes. We illustrate this idea in the following example.

Example 5: *Area ratio estimates*. We test the idea of using our findings on the eigenvalues of the normalized capacitance matrix to estimate the flow area ratio of permittivity distributions that are similar but not exactly as the three classes. The one on the left (denoted by ϵ_{test1}) of Figure 13 mimics a stratified flow, while the one on the right (denoted by ϵ_{test2}) mimics an eccentric flow.

We use normalization (6) in these examples. The first three eigenvalues of their normalized capacitance matrix $\tilde{\Xi}$ are

$$\epsilon_{\text{test1}} : \ \tau_1 = 7 \cdot 0942, \ \ \tau_2 = -2 \cdot 2893, \ \ \tau_3 = 0 \cdot 9607;$$
$$\epsilon_{\text{test2}} : \ \tau_1 = 3 \cdot 9834, \ \ \tau_2 = -2 \cdot 7648, \ \ \tau_3 = -2 \cdot 4549.$$
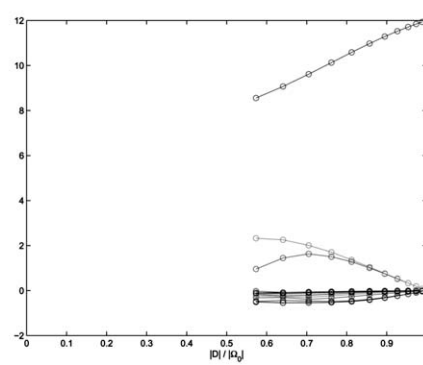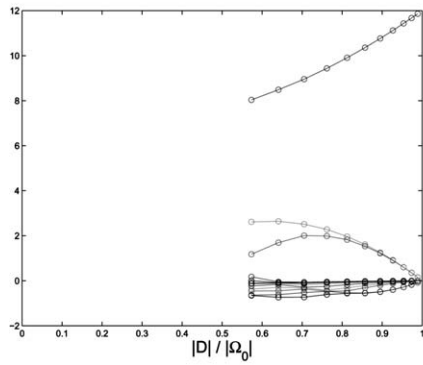
Using the characterization summarized above, we see that ϵ_{test1} indeed resembles a stratified flow, while ϵ_{test2} is similar to a core flow.

For ϵ_{test1}, we use stratified flows (21) as approximations to find an estimate for the area ratio $|D|/|\Omega_0|$. Since there is only one parameter d for this class, we use τ_1 from ϵ_{test1} to match with
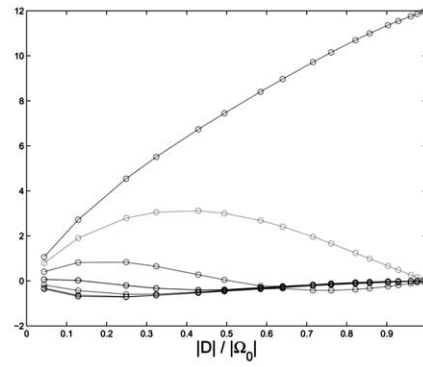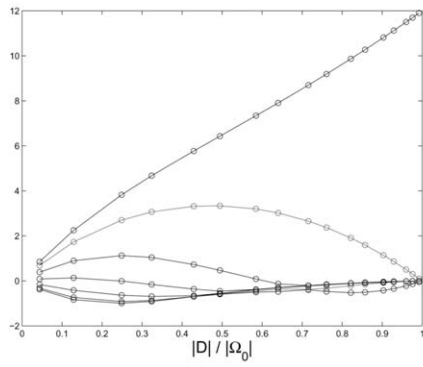
(a) Case of concentric annular flows: $d_0 = 0$.

(b) Case of eccentric annular flows: $d_0 = 0.3$.

Figure 10. The eigenvalues of Ξ (left) and $\tilde{\Xi}$ (right) plotted against the area ratio $|D|/|\Omega_0|$ for the annular flows (23), with $\theta_0 = 0$.
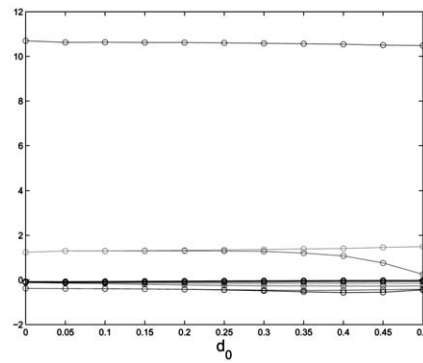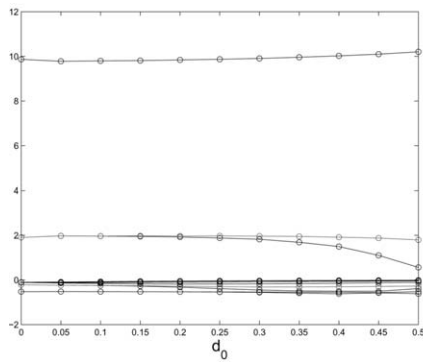

Figure 11. The eigenvalues of Ξ (left) and $\tilde{\Xi}$ (right) plotted against the eccentricity d_0 for the annular flows (23), with $r_0 = 0.4$ and $\theta_0 = 0$.
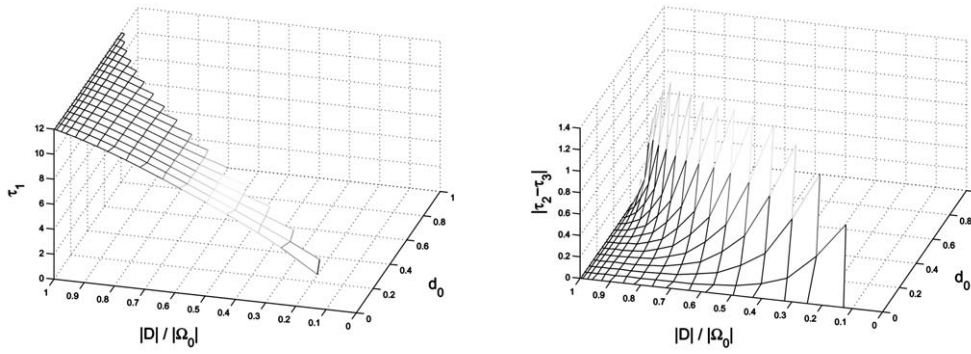
Figure 12. Surfaces of τ_1 (left) and $|\tau_2 - \tau_3|$ (right) for $\tilde{\Xi}$, as functions of eccentricity d_0 and area ratio $|D|/|\Omega_0|$, for the annular flows (23).

Figure 13. Test examples of permittivity distributions ϵ_{test1} (left) and ϵ_{test2} (right) that are not exactly within the three classes. The solid lines are our approximations by using the eigenvalues.

Table 1. Area ratio estimate for the test example ϵ_{test1}.

	ϵ_{test1}	stratified approximations	
		$d' = -0.12$	$d'' = -0.11$
τ_1	7·0942	7·0734	7·1229
		0·4177	0·4246
$|D|/|\Omega_0|$	**0·4213**	**0·4206** (by interpolation)	

that of a stratified flow. Matching is done through the following procedure: first, we find the two parameters d' and d'' such that τ_1 is contained in the corresponding interval $[\tau_1', \tau_1'']$, and then we use linear interpolation to find the area estimate for ρ from $[\rho', \rho'']$. The results are presented in Table 1. As can be seen, this method does provide an excellent estimate for the area ratio (relative error of 0·17%).

As for ϵ_{test2}, if we use only the concentric core flows ((22) with $d_0 = 0$) as approximations by simply matching up the leading eigenvalue τ_1, we would obtain an estimate for the area ratio with a relative error of about 9·44%. In the following, we illustrate how the use of $|\tau_2 - \tau_3|$ will effectively improve the area ratio estimate for this permittivity ϵ_{test2}. We use core flows (22) as approximations, and the two parameters, eccentricity d_0 and radius r_0, will both be used to

Table 2. Area ratio estimate for the test example ϵ_{test2}.

	ϵ_{test2}	core approximations			
		(d_0', r_0')	(d_0'', r_0')	(d_0', r_0'')	(d_0'', r_0'')
		$(0{\cdot}24, 0{\cdot}52)$	$(0{\cdot}26, 0{\cdot}52)$	$(0{\cdot}24, 0{\cdot}54)$	$(0{\cdot}26, 0{\cdot}54)$
τ_1	3·9834	3·7411	3·7977	4·0223	4·0852
$\lvert\tau_2 - \tau_3\rvert$	0·3129	0·2790	0·3280	0·2947	0·3446
		0·3284	0·3288	0·3547	0·3544
$\lvert D\rvert/\lvert\Omega_0\rvert$		0·3286 (by average)		0·3545 (by average)	
	0·3444	**0·3481** (by interpolation using τ_1)			

match τ_1 and $\lvert\tau_2-\tau_3\rvert$, and an alternate search strategy: search for r_0 to match τ_1, and search for d_0 to match $\lvert\tau_2 - \tau_3\rvert$. Starting with $d_0 = 0$, we search for the r_0 (with increment $\Delta r_0 = 0{\cdot}02$) whose corresponding τ_1 is the closest underestimate to that of ϵ_{test2}, and then, using this r_0, search for the d_0 (with increment $\Delta d_0 = 0{\cdot}02$) whose corresponding $\lvert\tau_2 - \tau_3\rvert$ is the closest underestimate of that of ϵ_{test2}, and so on. This process will terminate with the underestimate pair (d_0', r_0'). Repeat the process for the overestimate pair (d_0'', r_0''). We will also use the other pairs (d_0', r_0'') and (d_0'', r_0') for the estimate. These four pairs of parameter points can be actually determined by using pre-computed tables for τ_1 and $\lvert\tau_2 - \tau_3\rvert$ in terms of d_0 and r_0. From the leading eigenvalues τ_1 for these four pairs, we find an estimate for the area ratio by using linear interpolation in τ_1, after a simple averaging over d_0' and d_0''. The results are presented in Table 2. The estimate has a relative error of 1·07%, which is clearly an improvement over the case without using the eccentricity estimate.

6. Conclusions

Our main interest in this study has been to explore connections between capacitance data and the area ratio of permittivity contrast in electrical capacitance tomography. We formulated a mathematical model by using boundary-value problems for electric potentials in the sensor area. This model generated quantitative relations between the permittivity and the capacitance data, and, with these relations, we established some matrix properties of the capacitance data. Normalization of capacitance data is common in practice in helping extract permittivity information from the data, and we determined some matrix properties for normalized capacitance matrices. One particular result is that rotations in permittivity profile correspond to similar capacitance matrices. Since similar matrices have the same eigenvalue distribution and rotation of permittivity profile does not change the area ratio of permittivity contrast, we investigated the relation between the eigenvalues of normalized capacitance matrices and the area ratio of the permittivity distribution. We implemented a finite difference method to solve numerically the boundary-value problems in the more convenient polar coordinates. We specifically focused our investigation on the three common, practical classes of flows: stratified flows, core flows, and annular flows. Through numerical examples, we illustrated a strong correlation between the leading eigenvalue of the normalized capacitance matrices and the area ratio of the flow. We also found that the next two eigenvalues contain distinct-

ive information about the configuration of the flow among the three classes of permittivity distributions. In particular, for core and annular flows, the difference between the second and third eigenvalues was shown to be related to the eccentricity of the flow. These findings can be used to provide good estimates for the area ratio, and we demonstrated by numerical examples how this idea can be successfully implemented for some permittivities that are not exactly within these three classes. This estimation technique may also be applied to provide an excellent initial guess for iterative image reconstruction algorithms ([4]) thereby improving convergence of the reconstruction process.

Acknowledgements

References

1. W. Q. Yang, A. L. Stott and M. S. Beck, Development of capacitance tomographic imaging systems for oil pipeline measurements. *Rev. Sci. Instrum.* 66 (1995) 4326–4332.
2. T. A. York, Status of electrical tomography in industrial applications. *J. Electron. Imaging* 10 (2001) 608–619.
3. C. Gamio, A comparative analysis of single- and multiple-electrode excitation methods in electrical capacitance tomography. *Meas. Sci. Technol.* 13 (2002) 1799–1809.
4. W. Q. Yang and L. Peng, Image reconstruction algorithms for electrical capacitance tomography. *Meas. Sci. Technol.* 14 (2003) R1–R13.
5. D. Isaacson and M. Cheney, Effects of measurement precision and finite numbers of electrodes on linear impedance imaging algorithms. *SIAM J. Appl. Math.* 51 (1991) 1705–1731.
6. E. Somersalo, M. Cheney and D. Isaacson, Existence and uniqueness for electrode models for electric current computed tomography. *SIAM J. Appl. Math.* 52 (1992) 1023–1040.
7. D. C. Dobson and F. Santosa, Resolution and stability analysis of an inverse problem in electrical impedance tomography: dependence on the input current patterns. *SIAM J. Appl. Math.* 54 (1994) pp. 1542–1560.
8. M. Cheney, D. Isaacson and J. C. Newell, Electrical impedance tomography. *SIAM Rev.* 41 (1999) 85–101.
9. A. Tamburrino, S. Ventre and G. Rubinacci, Electrical resistance tomography: complementarity and quadratic models. *Inverse Problems* 16 (2000) 1585–1618.
10. A. Tamburrino and G. Rubinacci, A new non-iterative inversion method for electrical resistance tomography. *Inverse Problems* 18 (2002) 1809–1829.
11. G. Alessandrini, E. Rosset and J. K. Seo, Optimal size estimates for the inverse conductivity problem with one measurement. *Proc. Amer. Math. Soc.* 128 (1999) 53–64.
12. D. J. Griffiths, *Introduction to Electrodynamics* (3rd edtion). Upper Saddle River: Prentice Hall (1999) 576 pp.
13. W. Q. Yang and M. Byars, An improved normalisation approach for electrical capacitance tomography. In: *Proceedings of the 1st World Congress on Industrial Process Tomography* (1999) pp. 215–218.
14. G. Golub and C. Van Loan, *Matrix Computations* (3rd edition). Baltimore: Johns Hopkins University Press (1996) 694 pp.
15. A. Limon, A. Attiyah, L. Wu, E. Cumberbatch and C. Gamio, *Electric Capacitance Tomography*. Claremont: Mathematics Clinic Report, Claremont Graduate University (2003) 55 pp.